

# KIC 7914906: An Eclipsing Heartbeat Star with Tidally Excited Oscillations and Gamma Doradus/Delta Scuti Hybrid Pulsations

MIN-YU LI , <sup>1, 2, 3, 4</sup> SHENG-BANG QIAN , <sup>2, 3, \*</sup> LI-YING ZHU , <sup>1, 4, †</sup> WEN-PING LIAO , <sup>1, 4</sup> ER-GANG ZHAO, <sup>1, 4</sup>  
 XIANG-DONG SHI , <sup>1, 4</sup> FU-XING LI  AND QI-BIN SUN 

<sup>1</sup> Yunnan Observatories, Chinese Academy of Sciences, Kunming 650216, People's Republic of China

<sup>2</sup> Department of Astronomy, School of Physics and Astronomy, Yunnan University, Kunming 650091, People's Republic of China

<sup>3</sup> Key Laboratory of Astroparticle Physics of Yunnan Province, Yunnan University, Kunming 650091, People's Republic of China

<sup>4</sup> University of Chinese Academy of Sciences, No.1 Yangqihu East Road, Huairou District, Beijing 101408, People's Republic of China

## ABSTRACT

We present the eclipsing Heartbeat Star KIC 9704906 with tidally excited oscillations (TEOs) and gamma Doradus/delta Scuti hybrid pulsations. The derived parameters show that it has an orbital period of  $P=8.7529108(1)$  days, a high eccentricity of  $e=0.467(3)$ , and a high inclination of  $i=78^\circ.81(6)$ . The mass ratio  $q=0.981(5)$ , the relative radii (radius divided by semi-major axis)  $r_1=0.0639(2)$ , and  $r_2=0.0715(4)$  indicate that the secondary component has a less mass and a larger radius, and may have evolved off the main sequence. The eight derived TEO candidates,  $n = 3, 4, 5, 6, 7, 12, 40$ , and 44 harmonics, are consistent with or close to the dominant spherical harmonic  $l = 2$ ,  $m = 0$ , or  $\pm 2$ , assuming that the spin and orbital axes are aligned, and the pulsations are adiabatic and standing waves. We also identify ten independent frequency candidates, but one of them,  $f_7$ , is more like a modulation of a quasi-periodic signal and the orbits. According to the g-mode frequencies, we find that the rotation period of one component is 11.52(29) days. Although the masses and radii cannot be further constrained due to the lack of sufficient high-precision spectra, the fascinating phenomena in the Fourier spectra are evident and valuable in this system.

*Keywords:* Binary stars (154); Elliptical orbits (457); Stellar oscillations (1617)

## 1. INTRODUCTION

Pulsations are a powerful probe of the internal structure of stars using asteroseismology. The gamma Doradus ( $\gamma$  Dor) g mode, driven by the convective blocking mechanism (Guzik et al. 2000; Dupret et al. 2005), and the delta Scuti ( $\delta$  Sct) p mode, excited by the  $\kappa$  mechanism in the He II ionization zone (Gautschy & Saio 1995; Rodríguez & Breger 2001), are the two more common categories and they have been studied extensively (Bradley et al. 2015; Qian et al. 2018, 2019; Aerts et al. 2023). In addition, several systems exhibiting both  $\gamma$  Dor and  $\delta$  Sct properties have been reported (Handler & Shobbrook 2002; Grigahcène et al. 2010; Chapellier & Mathias 2013; Maceroni et al. 2014; Balona et al. 2015; Xiong et al. 2016; Schmid & Aerts 2016; Guo et al. 2017b; Helminiak et al. 2017; Lampens et al. 2018; Yang et al. 2021; Chen et al. 2024).

On the other hand, the tidally excited oscillations (TEOs; Zahn (1975); Kumar et al. (1995); Fuller (2017)) in Heartbeat Star (HBS) systems (Thompson et al. 2012) are induced by strong tidal effects during periastron passage in eccentric orbits. The main characteristic of TEOs is that they occur at exact integer multiples of the orbital frequency (Fuller 2017). So far, a number of papers have reported the TEOs in HBS systems (Welsh et al. 2011; Fuller & Lai 2012; Burkart et al. 2012; O'Leary & Burkart 2014; Hambleton et al. 2016; Guo et al. 2017a; Jayasinghe et al. 2019, 2021; Guo 2020; Guo et al. 2020; Cheng et al. 2020; Kołaczek-Szymański et al. 2021, 2022; Wrona et al. 2022; Guo et al. 2022; Wang et al. 2023; Li et al. 2024a).

However, pulsating stars with TEOs and  $\gamma$  Dor/ $\delta$  Sct hybrids are rare and interesting objects. Hambleton et al. (2013) reported KIC 4544587 with  $\delta$  Sct pulsations and TEOs. They identified 31 modes, including eight TEOs, six

\* E-mail: qiansb@ynu.edu.cn

† E-mail: zhuly@ynao.ac.cn

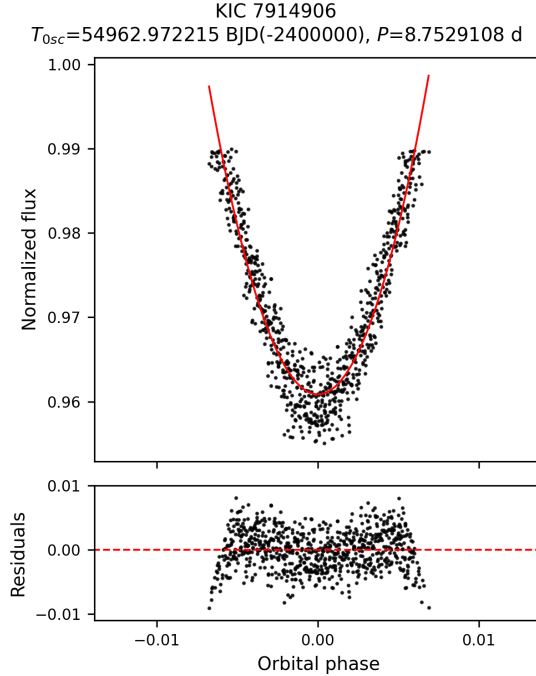


**Figure 1.** The upper panel shows the eclipse parts of the light curves (black dots) fit to a parabola (red solid line). The lower panel shows the residuals of the fit.

anharmonic g-mode  $\gamma$  Dor pulsation candidates, and 17 p-mode pulsations. Guo et al. (2019) studied the TEOs,  $\delta$  Sct p modes, and the self-driven  $\gamma$  Dor g modes in KIC 4142768. They derived the fundamental stellar properties of the HBS, which are in agreement with all the observations.

This paper presents the eclipsing HBS KIC 7914906, which exhibits TEOs and  $\gamma$  Dor/ $\delta$  Sct oscillations. Section 2 describes the binary modeling using the Kepler photometric data and the known atmospheric parameters. Section 3 performs a Fourier analysis of the residual light curve and discusses the pulsations, including the investigation of the TEOs, Gamma Doradus-type g modes, and Delta Scuti-type p and g modes. Section 4 summarizes and concludes our work.

## 2. BINARY MODELING

KIC 7914906 was reported as a HBS by Kirk et al. (2016) based on the long-term baseline and high-precision Kepler (Borucki et al. 2010) photometric data. They provide the raw and detrended data for  $\sim$ 30 minutes (long) cadence and raw  $\sim$ 1 minute (short) cadence data spanning from May 2009 to May 2013 in the online catalog<sup>1</sup>. We download the photometric data file and use the detrended data (Kirk et al. 2016) of all 18 quarters for our analysis.

In the first step, we fit the eclipsing parts of the light curves to a parabola,  $y = a(\frac{x-T_{0sc}}{P})^2 + c$ , where  $T_{0sc}$  is the time of superior conjunction, and  $P$  is the orbital period. As shown in Fig. 1, the black dots with phase range of (-0.01, 0.01) and the normalized flux less than 0.99 are considered as the eclipsing parts. We then obtain  $P=8.7529108(1)$  days and  $T_{0sc}=54962.972215(6)$  (BJD-2,400,000), which is very slightly different from that of Kirk et al. (2016) ( $P=8.7529074$ ,  $T_{0sc}=54962.971405$ ).

In the second step, we remove the eclipsing parts and fit the remaining parts of the light curves to the corrected Kumar et al. (1995) model (K95<sup>+</sup> model) following our previous work (Li et al. 2023). Although the K95<sup>+</sup> model is not suitable for eclipsing HBSs, we suggest that the eccentricity obtained from this approach is proper. We obtain an eccentricity  $e=0.518$ , which can be used for further constraints in the following step.

In the absence of sufficient high-precision spectra, we need to gather useful constraints on this system. Armstrong et al. (2014) have derived the effective temperatures,  $T_{\text{eff}1}=7227\pm365$  K and  $T_{\text{eff}2}=7223\pm651$  K, by fitting the spectral energy distribution. Huber et al. (2014) have obtained the effective temperature  $T_{\text{eff}}=7279^{+231}_{-322}$  K, the mass

<sup>1</sup> <http://keplerEBs.villanova.edu>

**Table 1.** Atmospheric Parameters from LAMOST

Parameter	pipe line 1	pipe line 2	pipe line 3
$T_{\text{eff}}$ (K)	7207(26)	7382(80)	7209(16)
log g	4.005(36)	3.869(130)	4.034(20)
[Fe/H]	-0.122(21)	-0.055(86)	-0.087(17)
RV (km/s)	-22.33(342)	-24.52(665)	-17.78(285)
Spec-Type	F0	F0	F0
DATE-OBS	2013-10-05T12:28:00	2014-05-22T19:50:00	2015-10-08T11:52:00
Phase	0.72	0.91	0.46

NOTE—The Spec-Type row is the spectral type. The DATE-OBS is the median observation time UTC. The phase is calculated according to the  $P$  and  $T_{0sc}$  derived in the first step. These results can be found at <https://www.lamost.org/dr7/>.

$M=1.800^{+0.273}_{-0.343} M_{\odot}$ , and the radius  $R=2.624^{+0.884}_{-0.778} R_{\odot}$  based on broadband photometry and asteroseismology. The Large Sky Area Multi-Object Fiber Spectroscopic Telescope (LAMOST, also called the Guo Shou Jing Telescope) (Wang et al. 1996; Luo et al. 2015) has provided three low-resolution spectra. The atmospheric parameters are listed in Table 1.

In the third step, we apply the binary model code PHysics Of Eclipsing BinariEs (PHOEBE, Prša et al. (2016); Prša (2018)) to the light curves using the emcee v3.1.4 Python package (Foreman-Mackey et al. 2013) based on the Markov Chain Monte Carlo (MCMC) method. Given the above atmospheric parameters, as well as the similar temperatures from Armstrong et al. (2014), and assuming that the two stars were born at similar times, we propose that both components are main sequence, with similar surface temperatures and similar masses. We also assume that the hotter component has an effective temperature of 7260 K, the mean of the effective temperatures above, and will fix it in the MCMC run.

In the first round of fitting, the priors of the parameters are set to uniform distributions. We fix  $T_{\text{eff}2}$  at 7260 K and set the temperature ratio  $\text{tratio}=T_{\text{eff}2}/T_{\text{eff}1}$  in the range (1.0, 1.1).<sup>2</sup> We set the mass ratio  $q=M_2/M_1$  in the range (0.9, 1.1), since we make no assumptions about which of the components is more massive. The eccentricity  $e$  is set in the range (0.4, 0.6) according to the result of the second step. The inclination  $i$  is set in the range ( $75^{\circ}$ ,  $85^{\circ}$ ) because of the obvious eclipse in the light curves. The argument of periastron  $\omega$  is set in the range ( $0^{\circ}$ ,  $180^{\circ}$ ). We just fix the semi-major axis sma to  $27 R_{\odot}$  according to the the mass reported by Huber et al. (2014). However, due to the lack of sufficient radial velocities (RVs), we can only constrain the the relative radii  $r_1$  and  $r_2$  based on the light curves alone, where  $r_1$  and  $r_2$  are the primary and secondary radii divided by the sma, respectively. The ranges of  $r_1$  and  $r_2$  are set in the range (0.06, 0.08). The  $T_{0sc}$  is set in the range (54962.97, 54962.98), a small range around the value derived in the first step. Both bolometric albedos,  $albedo_1$  and  $albedo_2$ , are set in the range (0.6, 0.8) according to the effective temperatures. Both gravity darkening coefficients,  $gdc_1$  and  $gdc_2$ , are set in the range (0.45, 1.0) according to the radiative envelope. The limb darkening coefficients are set in interpolated mode. The  $P$  is fixed at the value derived in the first step. Finally, we will simultaneously fit twelve parameters,  $e$ ,  $i$ ,  $\omega$ ,  $T_{0sc}$ ,  $q$ ,  $\text{tratio}$ ,  $r_1$ ,  $r_2$ ,  $albedo_1$ ,  $albedo_2$ ,  $gdc_1$ , and  $gdc_2$  in the MCMC run.

Since the fitting using the PHOEBE model is a very time-consuming procedure, we use 500 bins in phase to reduce the computation. In the MCMC run, we use 32 walkers and 5000 steps for a single chain. Then we obtain the convergence parameters. We then use the same walkers and steps in a single chain to derive the parameter uncertainties. The priors are set to be a normal distribution centered on the value from the previous step. Fig. 2 shows the fitting results, and Fig. A1 shows the corner plot of the MCMC fitting procedure. The parameters of the binary model are listed in Table 2.

<sup>2</sup> We find that the secondary is the hotter component in this scenario after trying several combinations of superparameters in the fitting procedures. Therefore, we fix the secondary temperature.

**Table 2.** Binary Model Parameters

Parameter	Value
Orbital Period, $P$ (days)	8.7529108(1)
Time of Superior Conjunction, $T_{0sc}$ (BJD')	54962.974666(50)
Time of Periastron, $T_{0p}$ (BJD')	54962.772581(50) <sup>b</sup>
eccentricity, $e$	0.467(3)
inclination, $i$ (degree)	78.81(6)
Argument of periastron, $\omega$ (degree)	64.66(7)
Mass ratio ( $M_2/M_1$ ), $q$	0.981(5)
Temperature ratio ( $T_{\text{eff}2}/T_{\text{eff}1}$ ), tratio	1.094(3)
$T_{\text{eff}1}$ (K)	6636(20)
$T_{\text{eff}2}$ (K)	7260 <sup>a</sup>
$r_1$ (sma)	0.0639(2)
$r_2$ (sma)	0.0715(4)
$albedo_1$	0.685(4)
$albedo_2$	0.686(5)
$gdc_1$	0.601(3)
$gdc_2$	0.749(2)

NOTE—The units of  $T_{0sc}$  and  $T_{0p}$  are BJD'=BJD−2,400,000.

<sup>a</sup> fixed.

<sup>b</sup> derived by the PHOEBE function.

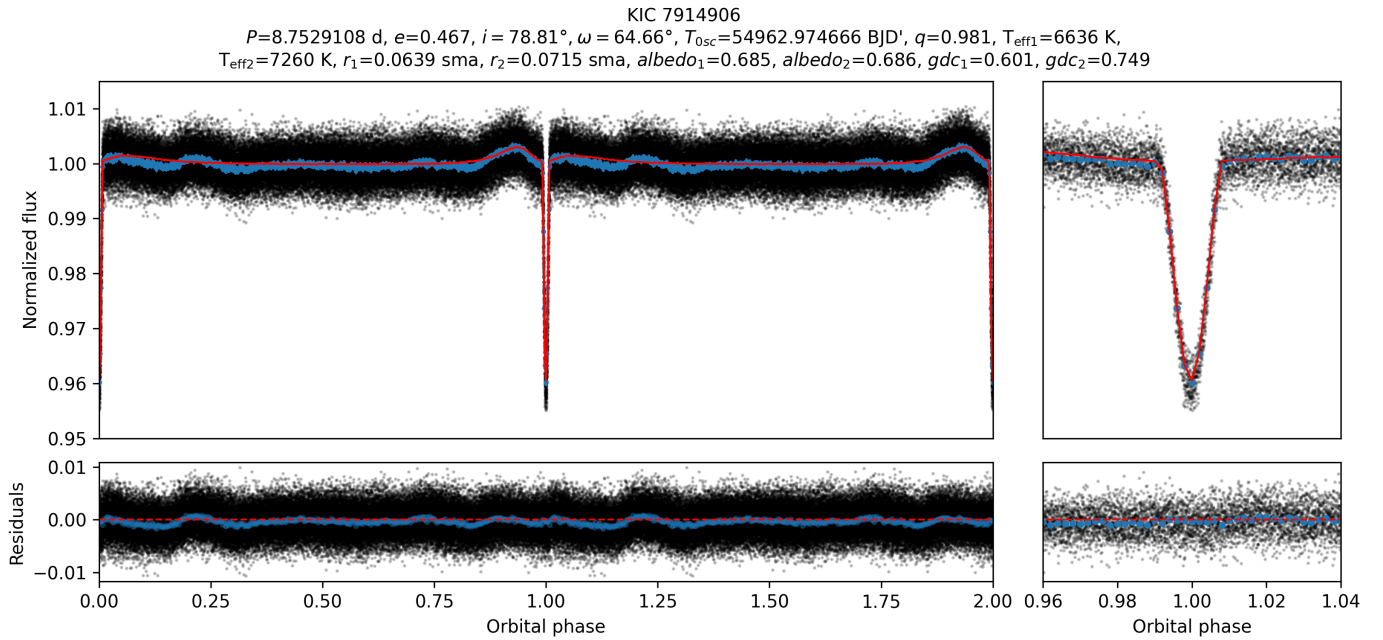


**Figure 2.** Fitting results for KIC 7914906. The PHOEBE model (solid red line) fitted to the phase-folded light curve (black dots) in the upper-left panel. The blue dots represent the phase-binned data. The lower-left panel shows the residuals of the fit. The dashed red line indicates a zero point. Note: The plot shows phases 0–2 to make the fitting results clear, and phases 1–2 are an exact copy of phases 0–1. The two right panels show zoomed light curves around eclipse.

### 3. PULSATION ANALYSIS

We perform the Fourier spectral analysis on the residuals of the light curve data, the black dots in the lower-left panel of Fig. 2, using the FNPEAKS<sup>3</sup> code-based analytic procedures. The flux variation is formulated as a sinusoidal

<sup>3</sup> <http://helas.astro.uni.wroc.pl/deliverables.php?active=fnpeaks>

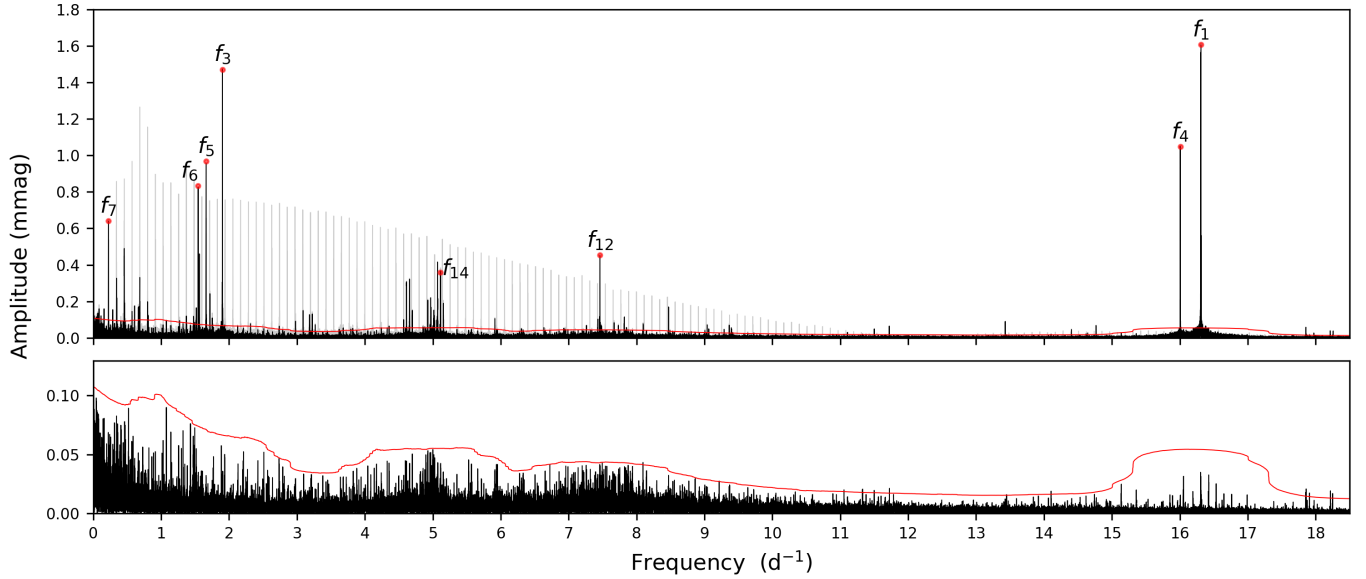


**Figure 3.** Upper panel: the Fourier spectrum of the residuals of the fit (black dots in the lower-left panel of Fig. 2). For comparison, the light gray curve is the Fourier spectrum of the original data (black dots in the upper-left panel of Fig. 2). Some independent frequencies in Table 3 are also labeled. Lower panel: the residual spectrum after removing the 209 detected frequencies. The red lines in both panels represent the amplitudes at  $S/N = 4.0$  as a function of frequency.

equation:

$$\sum A_i \sin[2\pi(f_i \cdot t + \phi_i)] \quad (1)$$

where  $A_i$ ,  $f_i$ , and  $\phi_i$  are the amplitude, frequency, and phase, respectively. The mean noise level of each frequency,  $N_i$ , is derived as the mean amplitude in the frequency range  $\pm 1 d^{-1}$ . The signal-to-noise ratio ( $S/N$ ) of the frequencies is  $A_i/N_i$ . We iteratively extract the peak frequencies until the  $S/N$  is no greater than 4.0 using Eq. (1)<sup>4</sup>. Uncertainties of frequencies, amplitudes and phases are estimated following Kallinger et al. (2008) (their Eqs. (1)~(4)). In addition, the time of each data point in the photometric light curves should subtract the time of periastron,  $T_{0p}$ , before Fourier analysis, where  $T_{0p}=54962.772581$  can be derived by the PHOEBE function according to the parameters obtained in Section 2. The purpose of adjusting the time of data points is to derive the correct phases of TEOs for the mode identification in Section 3.1 (Li et al. 2024b). Finally, a total of 209 frequencies are detected. Table 3 shows the ten independent frequency candidates; Table 4 shows the eight TEOs; Table A1 shows the other 191 combination frequencies or side lobes. When two frequencies are closer than the frequency resolution  $1.5/T_{span} \simeq 0.00103 d^{-1}$ , where  $T_{span}$  is the time span of about 1462 days of the Kepler data points, the frequency with the lower amplitude is identified as the possible side lobe. The combination frequencies in Table A1 also satisfy the requirement that the difference between the observed frequency and the value calculated by the equation in the Remark column is less than  $1.5/T_{span}$ . Fig. 3 shows the Fourier spectra. The Fourier spectrum of the residuals of the fit (black dots in the lower-left panel of Fig. 2) is shown in the upper panel. For comparison, the light gray curve is the Fourier spectrum of the original data (black dots in the upper-left panel of Fig. 2). The residual spectrum after removing the 209 detected frequencies is shown in the lower panel. We label only some of the independent frequencies, and detailed information is provided in the following sections.

<sup>4</sup> The fnpeaks code does not support phase derivation. However, it already derives the real and imaginary parts of the complex value of the Fourier transform results, and the phases can be calculated with minor modifications. The modified code can be downloaded from [https://github.com/MinyuLi/fnpeaks\\_phase](https://github.com/MinyuLi/fnpeaks_phase).

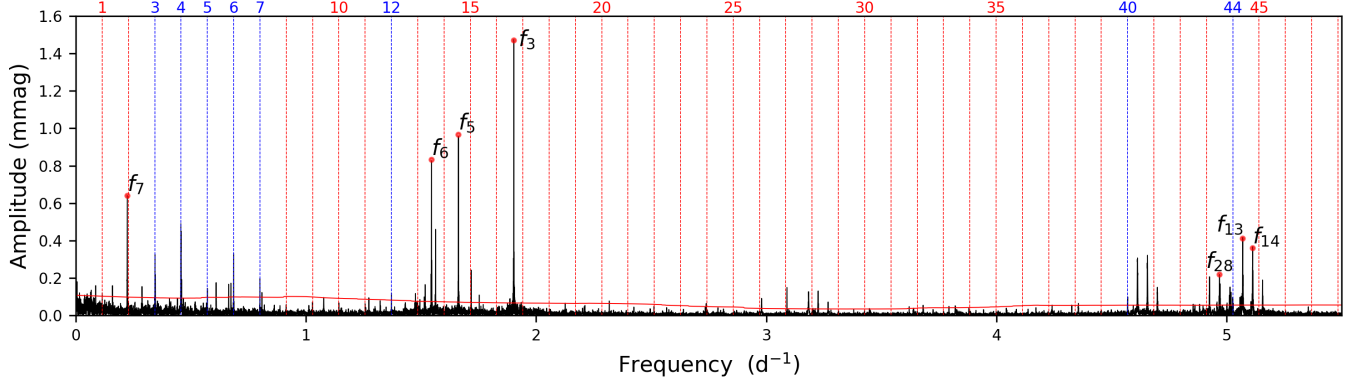


**Figure 4.** The Fourier spectrum in the range from 0 to 5.5 d<sup>-1</sup>. The red and blue vertical dashed lines represent the orbital harmonics  $n$ ; the blue ones indicate that they are TEOs. The solid red line shows the amplitudes at  $S/N = 4.0$  as a function of frequency. The independent frequency candidates less than 6 d<sup>-1</sup> in Table 3 are also labeled.

**Table 3.** Independent Frequency Candidates

ID	Freq.(d <sup>-1</sup> )	Ampl.(mmag)	S/N	Remark
$f_1$	16.3109249(20)	1.6070(84)	118.50	$\delta$ Sct
$f_3$	1.9028370(26)	1.472(10)	88.65	$\gamma$ Dor
$f_4$	16.0065308(30)	1.0485(84)	77.24	$\delta$ Sct
$f_5$	1.6621303(43)	0.968(11)	54.33	$\gamma$ Dor
$f_6$	1.5449563(52)	0.833(11)	45.07	$\gamma$ Dor
$f_7$	0.2231611(89)	0.641(15)	26.20	?
$f_{12}$	7.4603409(55)	0.4526(66)	42.16	$\delta$ Sct
$f_{13}$	5.0701402(78)	0.4126(85)	29.94	g-mode
$f_{14}$	5.1133239(90)	0.3596(85)	26.08	g-mode
$f_{28}$	4.968914(15)	0.2192(85)	15.90	g-mode

NOTE—The question mark in the Remark column of  $f_7$  indicates that it may not be an independent frequency, see text in Section 3.2.

**Table 4.** Tidally Excited Oscillations

ID	Freq. (d <sup>-1</sup> )	Ampl. (mmag)	Phase	S/N	$f/f_{\text{orb}}$	n
$f_9$	0.456217(11)	0.493(14)	0.164(9)	21.39	3.993	4
$f_{15}$	0.685465(17)	0.332(15)	0.274(15)	13.46	6.000	6
$f_{16}$	0.343769(17)	0.331(15)	0.760(14)	14.04	3.009	3
$f_{32}$	0.799714(28)	0.201(15)	0.219(24)	8.26	7.000	7
$f_{49}$	0.571215(38)	0.147(15)	0.478(32)	6.08	5.000	5
$f_{69}$	1.370997(39)	0.121(13)	0.005(33)	5.95	12.000	12
$f_{84}^a$	4.570127(31)	0.1038(85)	0.843(26)	7.58	40.002	40
$f_{87}^a$	5.026616(31)	0.1024(85)	0.171(27)	7.42	43.998	44

NOTE—Column  $n$  is the harmonic number of the TEO.

<sup>a</sup>  $f_{84}$  and  $f_{87}$  have third-order coupling modes, see text in Section 3.1.

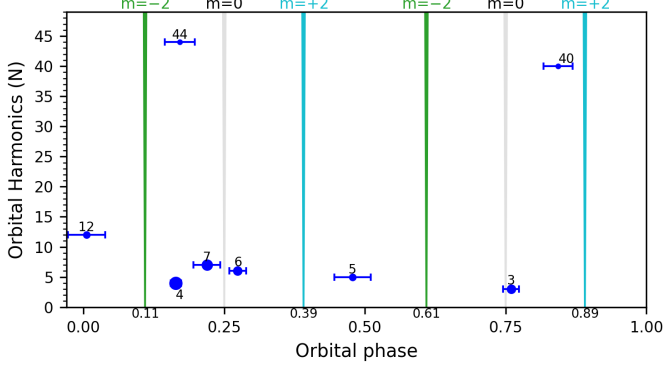


**Figure 5.** The pulsation phases of the TEOs. The gray, light blue, and green strips indicate the  $m = 0, +2$ , and  $-2$  modes, respectively. The phases of the  $m = +2, -2$  modes are shown near the strips. The blue circle represents a TEO with its harmonic number  $n$ ; the size corresponds to its amplitude; the error bar corresponds to the uncertainty of its phase.

### 3.1. Tidally Excited Oscillations

We use the analytic procedure reported in Li et al. (2024a) to detect the TEOs. As shown in the upper panel of Fig. 3, we apply Fourier transforms to the residuals (black curve) as well as to the original light curve (light gray curve). We consider the harmonic  $n$  to be a TEO if it occurs in both spectra. We also visually inspect all fits and exclude some frequencies with  $S/N < 5.0$  that may have been injected by imperfect model subtraction. Finally, the TEO candidates are the  $n = 4, 6, 3, 7, 5, 12, 40$ , and  $44$  harmonics. In addition, we also find two groups of third-order coupling modes for the harmonic  $n=40$ ,  $(f_6, f_{99}, f_{101})$  and  $(f_{36}, f_{47}, f_{61})$ , as well as five groups of third-order coupling modes for the  $n=44$  harmonic,  $(f_{11}, f_{71}, f_{191})$ ,  $(f_{30}, f_{44}, f_{71})$ ,  $(f_{36}, f_{51}, f_{142})$ ,  $(f_{36}, f_{101}, f_{117})$ , and  $(f_{58}, f_{67}, f_{101})$ . The harmonic TEO candidates are listed in Table 4.

In the theory of nonlinear mode coupling, when the TEO amplitudes exceed the parametric instability threshold, the TEOs begin to suffer from nonlinear mode coupling and transfer energy to daughter modes or multiple pairs of daughter modes (Weinberg et al. 2012; Yu et al. 2020; Guo 2021). Nonlinear mode coupling can explain the tidal oscillation frequencies of KOI-54, where the daughter modes have smaller amplitudes than their parents (O’Leary & Burkart 2014; Guo et al. 2022). Interestingly, the amplitudes of all the daughters are larger than those of their parents in KIC 7914906. Guo (2020) has identified two daughter modes with much larger amplitudes than the parent in KIC 3230227, suggesting that the nonlinear effect is a significant factor.

We then identify the pulsation phases and mode of these TEOs following Li et al. (2024b). The pulsation phases of the TEOs for dominant modes of spherical harmonic degree  $l = 2$  can be expressed by the equation (O’Leary & Burkart 2014; Guo et al. 2020) :

$$\phi_{l=2,m} = 0.25 + m\phi_0, \quad (2)$$

where azimuthal order  $m = 0, \pm 2$ ,  $\phi_0 = 0.25 - \omega/360^\circ$  and  $\omega$  is the argument of periastron. This equation holds under the following assumptions, including that the spin and orbital axes are aligned and that the pulsations are adiabatic and standing waves. As shown in Fig. 5, the gray, light blue, and green strips represent the theoretical pulsation phases  $\phi_m$  for  $m = 0, +2$ , and  $-2$  mode, respectively. The  $n = 3, 6$ , and  $7$  harmonics are consistent with the  $m = 0$  mode. The  $n = 4, 12$ , and  $44$  harmonics are close to the  $m = -2$  mode. The  $n = 5$  and  $40$  harmonics are close to the  $m = 2$  mode.

### 3.2. Gamma Doradus-type g Modes

$\gamma$  Dor stars are characterized by low-frequency g-mode pulsations with masses ranging from  $1.3$  to  $2.0$   $M_\odot$  and periods of about  $0.3$  to  $3$  days (Qian et al. 2019; Guo et al. 2019). As can be seen in Fig. 4 and Table 3,  $f_3, f_5, f_6$ , and  $f_7$  are the self-excited  $\gamma$  Dor frequencies candidates. Since  $f_{11}$  is too close to  $f_6$ , we suggest that it is not an independent frequency.

The  $f_7 \approx 1.95 f_{\text{orb}}$  is not an exact integer multiple of the orbital frequency. However, since it is easily related to the orbit, we examine whether the frequency changes during all quarters. We slice the photometric data into segments,

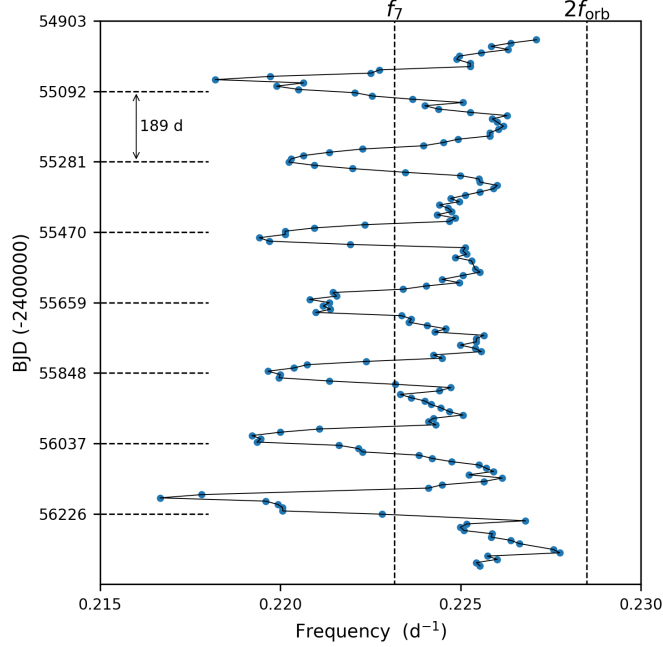


**Figure 6.** Change in peak value of  $f_7$  over time. The blue dots represent the frequency peak for each data segment. The two vertical dashed lines represent the  $f_7$  value in Table 3 and the  $2f_{\text{orb}}$ , respectively. The horizontal dashed lines represent the quasi-periodic interval of 189 days.

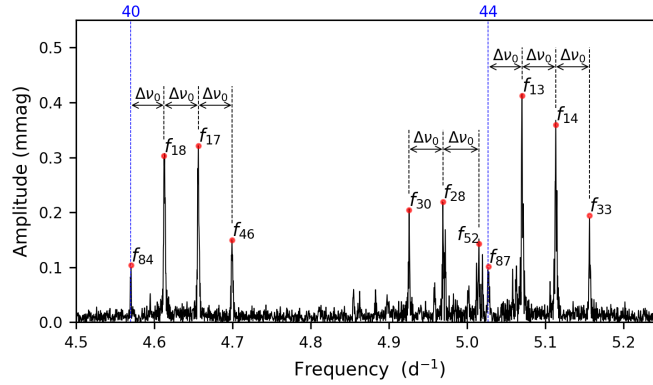


**Figure 7.** The details of the frequency range of  $4.5 \sim 5.25 \text{ d}^{-1}$ .

each starting at an interval of one orbital period and spanning 87 days (about ten orbital periods). We then extract the frequency peak around  $(0.21 \text{ d}^{-1}, 0.23 \text{ d}^{-1})$  for each data segment by Fourier transform. As shown in Fig. 6, the frequencies are changing. In addition, there is a quasi-periodicity in their changes. We also perform a Fourier transform on these peak frequencies and find that the quasi-periodic interval is about 189 days. We therefore suggest that  $f_7$  is a modulation of some quasi-periodic signal and the orbits, rather than an independent frequency.

Furthermore, no changes were found in  $f_3$ ,  $f_5$ , and  $f_6$  after the same examination. Therefore, they are independent frequencies.

### 3.3. Delta Scuti-type p and g Modes

The  $\delta$  Sct stars lie in the classical Cepheid instability strip with masses from 1.5 to  $3 M_{\odot}$  and spectral types from A2 to F5. They exhibit both radial and non-radial pulsations with frequencies ranging from 3 to  $80 \text{ d}^{-1}$  and can oscillate in both p and g modes (Qian et al. 2018). The  $f_1$  and  $f_4$  in Fig. 3 are typical  $\delta$  Sct p modes. Since  $f_2$  and  $f_8$  are too close to  $f_1$ , we suggest that they are not independent frequencies. In addition,  $f_{12}$  and the frequencies around  $5 \text{ d}^{-1}$  (Figs. 3 and 4) are g-mode pulsations.

However, there are three groups of g-mode frequencies in the frequency range of around  $5 \text{ d}^{-1}$  that are very noteworthy. Fig. 7 shows the details of these three frequency groups:  $(f_{84}, f_{18}, f_{17}, f_{46})$ ,  $(f_{30}, f_{28}, f_{52})$ , and  $(f_{87}, f_{13}, f_{14}, f_{33})$ . The space between two adjacent frequencies is  $\Delta\nu_0=0.0434(11)$ . Among these frequencies,  $f_{84}$  and  $f_{87}$  are harmonic TEOs;  $f_{13}$ ,  $f_{14}$ , and  $f_{28}$  are independent frequencies. This may be a rotational variable with splitting caused by the proximity effect. In particular, the splitting of high-order g modes of degree 1 is only half the rotation rate (Aerts et al. 2010). Therefore, we propose that the rotation period of the one component is  $P_{rot}=(2\Delta\nu_0)^{-1}=11.52(29)$  d, but it is not yet clear to which component this rotation period belongs. Given the high eccentricity of this system, we expect that at least one component is not tidally locked. That the rotation period is different from the orbital period is not surprising.

## 4. SUMMARY AND CONCLUSIONS

In this work, we study the eclipsing HBS KIC 7914906. We apply the PHOEBE binary model code to the light curves using the MCMC method. The derived orbital period  $P=8.7529108(1)$  days, eccentricity  $e=0.467(3)$ , inclination  $i=78^{\circ}.81(6)$ , mass ratio  $q=0.981(5)$ ,  $T_{\text{eff}1}=6636(20)$  K,  $T_{\text{eff}2}=7260$  K, the relative radii  $r_1=0.0639(2)$  sma and  $r_2=0.0715(4)$  sma. This indicates that the secondary is the less massive and hotter component with a larger radius, and may have evolved off the main sequence.

The Fourier spectral analysis shows that KIC 7914906 exhibits the TEOs,  $\gamma$  Dor and  $\delta$  Sct hybrid pulsations. We extract 209 frequencies with  $S/N \gtrsim 4.0$ , including ten independent frequency candidates, eight TEO candidates, and 191 combination frequencies or side lobes. According to the pulsation phases and mode identification, the  $n = 3$ , 6, and 7 harmonics are spherical harmonic degree  $l = 2$  and azimuthal order  $m = 0$  mode; the  $n = 4$ , 12, and 44 harmonics are  $l = 2$  and  $m = -2$  mode; the  $n = 5$  and 40 harmonics are  $l = 2$  and  $m = 2$  mode. We also find the rotation period of one component, which is 11.52(29) days. The  $f_7 \approx 1.95 f_{\text{orb}}$  is also interesting in this system. We find that it is a modulation of a quasi-periodic signal with about 189 days and the orbits.

Since the absence of sufficient high-precision spectra, masses and radii cannot be further constrained. However, the fascinating phenomena in the Fourier spectra are evident and valuable. We leave high-precision spectroscopic observations for future work, when the power of asteroseismology can reveal more of the internal structure of this system.

## 5. ACKNOWLEDGMENTS

This work is partly supported by the National Key R&D Program of China (Grant No. 2022YFE0116800), the National Natural Science Foundation of China (Nos. 11933008 and 12103084), the Basic Research Project of Yunnan Province (Grant Nos. 202201AT070092 and 202301AT070352), the Science Foundation of Yunnan Province (No. 202401AS070046), and the Yunnan Revitalization Talent Support Program. We are grateful to Kirk et al. (2016) for their excellent work and for sharing the results of their work. Funding for the Kepler mission is provided by the NASA Science Mission directorate. The Guoshoujing Telescope (the Large Sky Area Multi-Object Fiber Spectroscopic Telescope LAMOST) is a National Major Scientific Project built by the Chinese Academy of Sciences. We thank the Kepler and LAMOST teams for their support and hard work. We thank the anonymous referee for constructive comments that have been a source of improvement for this manuscript.

*Software:* FNPEAKS (Z. Koołaczkowski, W. Hebisch, G. Kopacki), PHOEBE (Prša et al. 2016), emcee (Foreman-Mackey et al. 2013).

## REFERENCES

- |   |   |
|---|---|
| Aerts, C., Christensen-Dalsgaard, J., & Kurtz, D. W. 2010,<br>Astroseismology, doi: <a href="https://doi.org/10.1007/978-1-4419-5803-5">10.1007/978-1-4419-5803-5</a> | Aerts, C., Molenberghs, G., & De Ridder, J. 2023, A&A,<br>672, A183, doi: <a href="https://doi.org/10.1051/0004-6361/202245713">10.1051/0004-6361/202245713</a> |
|---|---|

- Armstrong, D. J., Gómez Maqueo Chew, Y., Faedi, F., & Pollacco, D. 2014, MNRAS, 437, 3473, doi: [10.1093/mnras/stt2146](https://doi.org/10.1093/mnras/stt2146)
- Balona, L. A., Daszyńska-Daszkiewicz, J., & Pamyatnykh, A. A. 2015, MNRAS, 452, 3073, doi: [10.1093/mnras/stv1513](https://doi.org/10.1093/mnras/stv1513)
- Borucki, W. J., Koch, D., Basri, G., et al. 2010, Science, 327, 977, doi: [10.1126/science.1185402](https://doi.org/10.1126/science.1185402)
- Bradley, P. A., Guzik, J. A., Miles, L. F., et al. 2015, AJ, 149, 68, doi: [10.1088/0004-6256/149/2/68](https://doi.org/10.1088/0004-6256/149/2/68)
- Burkart, J., Quataert, E., Arras, P., & Weinberg, N. N. 2012, MNRAS, 421, 983, doi: [10.1111/j.1365-2966.2011.20344.x](https://doi.org/10.1111/j.1365-2966.2011.20344.x)
- Chapellier, E., & Mathias, P. 2013, A&A, 556, A87, doi: [10.1051/0004-6361/201321907](https://doi.org/10.1051/0004-6361/201321907)
- Chen, X., Zhang, X., Li, Y., & Su, J. 2024, ApJ, 963, 155, doi: [10.3847/1538-4357/ad2266](https://doi.org/10.3847/1538-4357/ad2266)
- Cheng, S. J., Fuller, J., Guo, Z., Lehman, H., & Hambleton, K. 2020, ApJ, 903, 122, doi: [10.3847/1538-4357/abb46d](https://doi.org/10.3847/1538-4357/abb46d)
- Dupret, M. A., Grigahcène, A., Garrido, R., Gabriel, M., & Scuflaire, R. 2005, A&A, 435, 927, doi: [10.1051/0004-6361:20041817](https://doi.org/10.1051/0004-6361:20041817)
- Foreman-Mackey, D., Hogg, D. W., Lang, D., & Goodman, J. 2013, PASP, 125, 306, doi: [10.1086/670067](https://doi.org/10.1086/670067)
- Fuller, J. 2017, MNRAS, 472, 1538, doi: [10.1093/mnras/stx2135](https://doi.org/10.1093/mnras/stx2135)
- Fuller, J., & Lai, D. 2012, MNRAS, 420, 3126, doi: [10.1111/j.1365-2966.2011.20237.x](https://doi.org/10.1111/j.1365-2966.2011.20237.x)
- Gautschy, A., & Saio, H. 1995, ARA&A, 33, 75, doi: [10.1146/annurev.aa.33.090195.000451](https://doi.org/10.1146/annurev.aa.33.090195.000451)
- Grigahcène, A., Antoci, V., Balona, L., et al. 2010, ApJL, 713, L192, doi: [10.1088/2041-8205/713/2/L192](https://doi.org/10.1088/2041-8205/713/2/L192)
- Guo, Z. 2020, ApJ, 896, 161, doi: [10.3847/1538-4357/ab911f](https://doi.org/10.3847/1538-4357/ab911f)
- . 2021, Frontiers in Astronomy and Space Sciences, 8, 67, doi: [10.3389/fspas.2021.663026](https://doi.org/10.3389/fspas.2021.663026)
- Guo, Z., Fuller, J., Shporer, A., et al. 2019, ApJ, 885, 46, doi: [10.3847/1538-4357/ab41f6](https://doi.org/10.3847/1538-4357/ab41f6)
- Guo, Z., Gies, D. R., & Fuller, J. 2017a, ApJ, 834, 59, doi: [10.3847/1538-4357/834/1/59](https://doi.org/10.3847/1538-4357/834/1/59)
- Guo, Z., Gies, D. R., & Matson, R. A. 2017b, ApJ, 851, 39, doi: [10.3847/1538-4357/aa978c](https://doi.org/10.3847/1538-4357/aa978c)
- Guo, Z., Ogilvie, G. I., Li, G., Townsend, R. H. D., & Sun, M. 2022, MNRAS, 517, 437, doi: [10.1093/mnras/stac2611](https://doi.org/10.1093/mnras/stac2611)
- Guo, Z., Shporer, A., Hambleton, K., & Isaacson, H. 2020, ApJ, 888, 95, doi: [10.3847/1538-4357/ab58c2](https://doi.org/10.3847/1538-4357/ab58c2)
- Guzik, J. A., Kaye, A. B., Bradley, P. A., Cox, A. N., & Neuforege, C. 2000, ApJL, 542, L57, doi: [10.1086/312908](https://doi.org/10.1086/312908)
- Hambleton, K., Kurtz, D. W., Prša, A., et al. 2016, MNRAS, 463, 1199, doi: [10.1093/mnras/stw1970](https://doi.org/10.1093/mnras/stw1970)
- Hambleton, K. M., Kurtz, D. W., Prša, A., et al. 2013, MNRAS, 434, 925, doi: [10.1093/mnras/stt886](https://doi.org/10.1093/mnras/stt886)
- Handler, G., & Shobbrook, R. R. 2002, MNRAS, 333, 251, doi: [10.1046/j.1365-8711.2002.05401.x](https://doi.org/10.1046/j.1365-8711.2002.05401.x)
- Hełminiak, K. G., Ukita, N., Kambe, E., et al. 2017, A&A, 602, A30, doi: [10.1051/0004-6361/201630379](https://doi.org/10.1051/0004-6361/201630379)
- Huber, D., Silva Aguirre, V., Matthews, J. M., et al. 2014, ApJS, 211, 2, doi: [10.1088/0067-0049/211/1/2](https://doi.org/10.1088/0067-0049/211/1/2)
- Jayasinghe, T., Stanek, K. Z., Kochanek, C. S., et al. 2019, MNRAS, 489, 4705, doi: [10.1093/mnras/stz2460](https://doi.org/10.1093/mnras/stz2460)
- Jayasinghe, T., Kochanek, C. S., Strader, J., et al. 2021, MNRAS, 506, 4083, doi: [10.1093/mnras/stab1920](https://doi.org/10.1093/mnras/stab1920)
- Kallinger, T., Reegen, P., & Weiss, W. W. 2008, A&A, 481, 571, doi: [10.1051/0004-6361:20077559](https://doi.org/10.1051/0004-6361:20077559)
- Kirk, B., Conroy, K., Prša, A., et al. 2016, AJ, 151, 68, doi: [10.3847/0004-6256/151/3/68](https://doi.org/10.3847/0004-6256/151/3/68)
- Kołaczek-Szymański, P. A., Pigulski, A., Michalska, G., Moździerski, D., & Różański, T. 2021, A&A, 647, A12, doi: [10.1051/0004-6361/202039553](https://doi.org/10.1051/0004-6361/202039553)
- Kołaczek-Szymański, P. A., Pigulski, A., Wrona, M., Ratajczak, M., & Udałski, A. 2022, A&A, 659, A47, doi: [10.1051/0004-6361/202142171](https://doi.org/10.1051/0004-6361/202142171)
- Kumar, P., Ao, C. O., & Quataert, E. J. 1995, ApJ, 449, 294, doi: [10.1086/176055](https://doi.org/10.1086/176055)
- Lampens, P., Frémat, Y., Vermeylen, L., et al. 2018, A&A, 610, A17, doi: [10.1051/0004-6361/201730694](https://doi.org/10.1051/0004-6361/201730694)
- Li, M.-Y., Qian, S.-B., Zhu, L.-Y., et al. 2023, ApJS, 266, 28, doi: [10.3847/1538-4365/acca13](https://doi.org/10.3847/1538-4365/acca13)
- . 2024a, ApJ, 962, 44, doi: [10.3847/1538-4357/ad18c1](https://doi.org/10.3847/1538-4357/ad18c1)
- . 2024b, MNRAS, 530, 586, doi: [10.1093/mnras/stae885](https://doi.org/10.1093/mnras/stae885)
- Luo, A. L., Zhao, Y.-H., Zhao, G., et al. 2015, Research in Astronomy and Astrophysics, 15, 1095, doi: [10.1088/1674-4527/15/8/002](https://doi.org/10.1088/1674-4527/15/8/002)
- Maceroni, C., Lehmann, H., da Silva, R., et al. 2014, A&A, 563, A59, doi: [10.1051/0004-6361/201322871](https://doi.org/10.1051/0004-6361/201322871)
- O’Leary, R. M., & Burkart, J. 2014, MNRAS, 440, 3036, doi: [10.1093/mnras/stu335](https://doi.org/10.1093/mnras/stu335)
- Prša, A. 2018, Modeling and Analysis of Eclipsing Binary Stars: The theory and design principles of PHOEBE, doi: [10.1088/978-0-7503-1287-5](https://doi.org/10.1088/978-0-7503-1287-5)
- Prša, A., Conroy, K. E., Horvat, M., et al. 2016, ApJS, 227, 29, doi: [10.3847/1538-4365/227/2/29](https://doi.org/10.3847/1538-4365/227/2/29)
- Qian, S. B., Li, L. J., He, J. J., et al. 2018, MNRAS, 475, 478, doi: [10.1093/mnras/stx3185](https://doi.org/10.1093/mnras/stx3185)
- Qian, S.-B., Li, L.-J., He, J.-J., et al. 2019, Research in Astronomy and Astrophysics, 19, 001, doi: [10.1088/1674-4527/19/1/1](https://doi.org/10.1088/1674-4527/19/1/1)
- Rodríguez, E., & Breger, M. 2001, A&A, 366, 178, doi: [10.1051/0004-6361:20000205](https://doi.org/10.1051/0004-6361:20000205)

- Schmid, V. S., & Aerts, C. 2016, A&A, 592, A116, doi: [10.1051/0004-6361/201628617](https://doi.org/10.1051/0004-6361/201628617)
- Thompson, S. E., Everett, M., Mullally, F., et al. 2012, ApJ, 753, 86, doi: [10.1088/0004-637X/753/1/86](https://doi.org/10.1088/0004-637X/753/1/86)
- Wang, K., Ren, A., Andersen, M. F., et al. 2023, AJ, 166, 42, doi: [10.3847/1538-3881/acdac9](https://doi.org/10.3847/1538-3881/acdac9)
- Wang, S.-G., Su, D.-Q., Chu, Y.-Q., Cui, X., & Wang, Y.-N. 1996, ApOpt, 35, 5155, doi: [10.1364/AO.35.005155](https://doi.org/10.1364/AO.35.005155)
- Weinberg, N. N., Arras, P., Quataert, E., & Burkart, J. 2012, ApJ, 751, 136, doi: [10.1088/0004-637X/751/2/136](https://doi.org/10.1088/0004-637X/751/2/136)
- Welsh, W. F., Orosz, J. A., Aerts, C., et al. 2011, ApJS, 197, 4, doi: [10.1088/0067-0049/197/1/4](https://doi.org/10.1088/0067-0049/197/1/4)
- Wrona, M., Kołaczek-Szymański, P. A., Ratajczak, M., & Kozłowski, S. 2022, ApJ, 928, 135, doi: [10.3847/1538-4357/ac56e6](https://doi.org/10.3847/1538-4357/ac56e6)
- Xiong, D. R., Deng, L., Zhang, C., & Wang, K. 2016, MNRAS, 457, 3163, doi: [10.1093/mnras/stw047](https://doi.org/10.1093/mnras/stw047)
- Yang, T.-Z., Zuo, Z.-Y., Li, G., et al. 2021, A&A, 655, A63, doi: [10.1051/0004-6361/202142198](https://doi.org/10.1051/0004-6361/202142198)
- Yu, H., Weinberg, N. N., & Fuller, J. 2020, MNRAS, 496, 5482, doi: [10.1093/mnras/staa1858](https://doi.org/10.1093/mnras/staa1858)
- Zahn, J. P. 1975, A&A, 41, 329

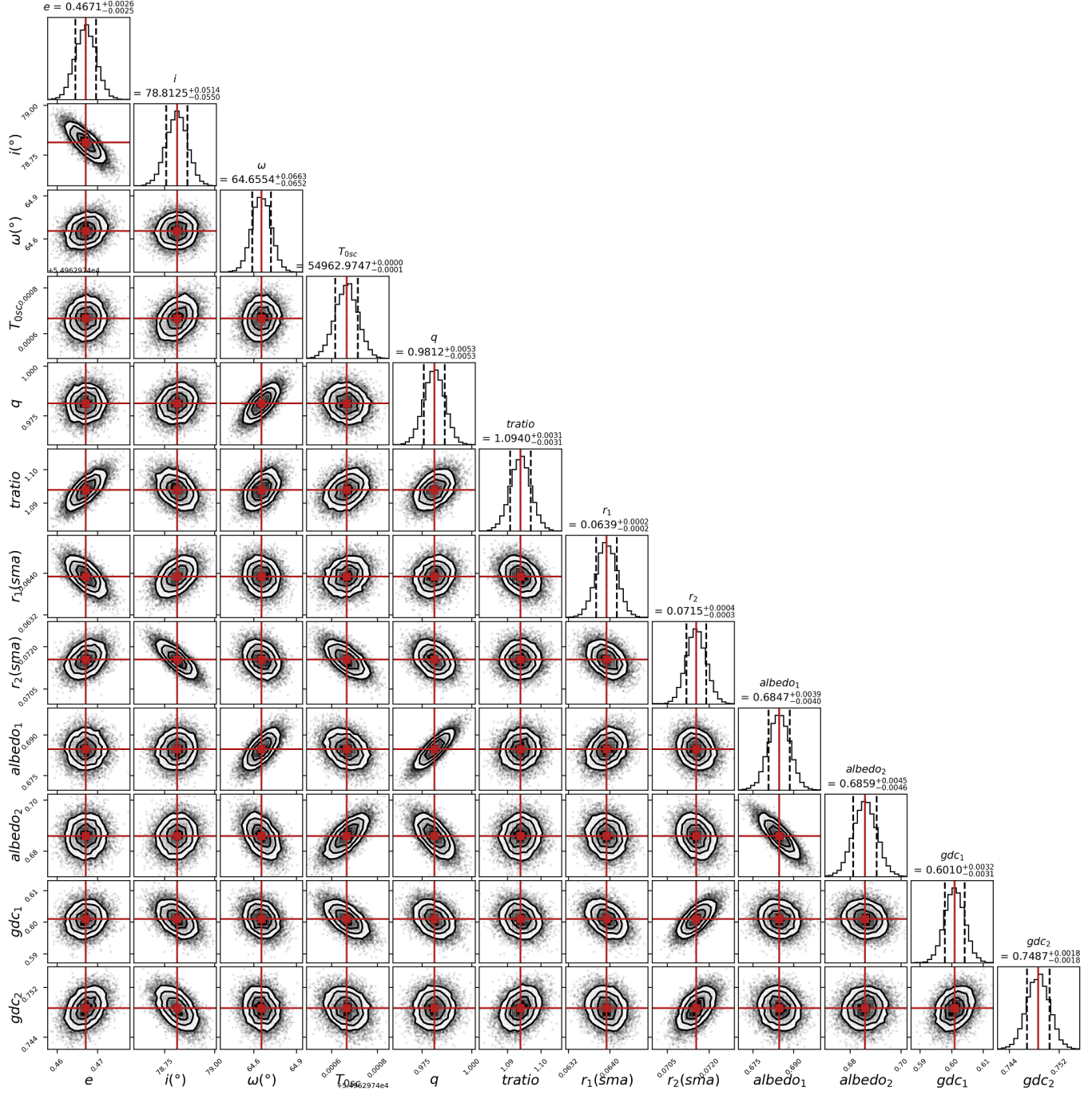


**Figure A1.** Corner plot of the MCMC fit procedure for KIC 7914906. Red vertical lines indicate the median values of the presented histograms for each parameter. Black vertical dashed lines show  $1 \sigma$  uncertainties.

## APPENDIX

Fig. A1 shows the corner plot of the MCMC fit procedure.

**Table A1.** Possible Combination or Side Lobe Frequencies

ID	Freq.(d <sup>-1</sup> )	Ampl.(mmag)	S/N	Remark	ID	Freq.(d <sup>-1</sup> )	Ampl.(mmag)	S/N	Remark
$f_2$	16.3058925(21)	1.5206(84)	112.11	$f_1 - f_{36}$	$f_8$	16.3148352(60)	0.5288(84)	39.00	$f_1 + 2f_{63}$
$f_{10}$	0.457169(11)	0.485(14)	21.07	side lobe	$f_{11}$	1.5629099(94)	0.456(11)	24.81	$f_6 + 8f_{63}$
$f_{17}$	4.6562568(100)	0.3208(85)	23.41	$f_{14} - 4f_{\text{orb}}$	$f_{18}$	4.612393(11)	0.3029(85)	22.03	$\simeq f_{13} - 4f_{\text{orb}}$
$f_{19}$	4.613107(11)	0.3020(85)	21.97	side lobe	$f_{20}$	5.069528(11)	0.2949(85)	21.40	side lobe
$f_{21}$	4.655475(11)	0.2808(85)	20.49	side lobe	$f_{22}$	5.112542(13)	0.2556(85)	18.53	side lobe
$f_{23}$	5.071806(13)	0.2424(85)	17.59	$f_4 - 4f_7$	$f_{24}$	1.717997(17)	0.241(11)	14.00	$f_5 + 11f_{36}$
$f_{25}$	5.114820(14)	0.2345(85)	17.00	$f_6 + 16f_7$	$f_{26}$	0.345402(25)	0.223(15)	9.45	$f_{16} + f_{63}$
$f_{27}$	4.613821(14)	0.2216(85)	16.12	$f_{13} - f_9$	$f_{29}$	0.222345(27)	0.215(15)	8.77	side lobe
$f_{30}$	4.925798(16)	0.2045(85)	14.94	$f_{32} + 12f_{16}$	$f_{31}$	1.546690(21)	0.203(11)	10.97	$f_{17} - 9f_{26}$
$f_{33}$	5.156406(17)	0.1946(85)	14.10	$f_{24} + 10f_{16}$	$f_{34}$	0.223807(30)	0.190(15)	7.77	side lobe
$f_{35}$	0.457883(29)	0.188(14)	8.15	$f_{13} - f_{18}$	$f_{36}$	0.005134(35)	0.180(17)	6.69	$f_1 - f_2$
$f_{37}$	0.609400(31)	0.179(15)	7.43	$f_{15} - 15f_{36}$	$f_{38}$	1.517720(25)	0.173(12)	9.25	$f_{11} - 9f_{36}$
$f_{39}$	0.673768(33)	0.172(15)	6.97	$f_{49} + 20f_{36}$	$f_{40}$	8.472166(12)	0.1690(56)	18.71	$f_{25} + 39f_{44}$
$f_{41}$	4.656835(19)	0.1669(85)	12.18	side lobe	$f_{42}$	0.663941(35)	0.163(15)	6.62	$f_{15} - 4f_{36}$
$f_{43}$	0.287223(35)	0.161(15)	6.70	$f_5 - 4f_{16}$	$f_{44}$	0.086061(38)	0.160(16)	6.15	$f_{28} - 17f_{43}$
$f_{45}$	7.460953(16)	0.1576(66)	14.68	side lobe	$f_{46}$	4.699270(21)	0.1499(85)	10.96	$f_{18} + f_{44}$
$f_{47}$	3.089845(14)	0.1491(55)	16.68	$f_{36} + 27f_{\text{orb}}$	$f_{48}$	4.969492(22)	0.1470(85)	10.65	side lobe
$f_{50}$	4.611747(22)	0.1453(85)	10.57	side lobe	$f_{51}$	0.159032(41)	0.144(16)	5.70	$f_{16} - 36f_{36}$
$f_{52}$	5.015022(23)	0.1428(85)	10.36	$f_{28} + 9f_{36}$	$f_{53}$	5.071024(23)	0.1402(85)	10.17	side lobe
$f_{54}$	0.066850(44)	0.140(16)	5.36	$f_{51} - 18f_{36}$	$f_{55}$	7.458709(18)	0.1393(66)	12.98	$f_{38} + 52f_{\text{orb}}$
$f_{56}$	0.459311(39)	0.137(14)	5.95	$f_5 - 18f_{54}$	$f_{57}$	4.972008(24)	0.1368(85)	9.91	$f_6 + 5f_{15}$
$f_{58}$	3.225244(15)	0.1328(54)	15.35	$f_5 + f_{11}$	$f_{59}$	4.698556(24)	0.1309(85)	9.57	side lobe
$f_{60}$	3.183659(16)	0.1264(54)	14.43	$f_{28} - 8f_7$	$f_{61}$	1.475522(35)	0.125(12)	6.59	$f_{11} - 17f_{36}$
$f_{62}$	4.699951(26)	0.1236(85)	9.04	side lobe	$f_{63}$	0.002244(51)	0.123(17)	4.57	$f_{56} - 4f_{\text{orb}}$
$f_{64}$	0.037539(51)	0.123(16)	4.62	$f_7 - 36f_{36}$	$f_{65}$	0.808419(46)	0.122(15)	5.03	$f_{32} + 4f_{63}$
$f_{66}$	5.019680(26)	0.1220(85)	8.85	$f_{13} - 10f_{36}$	$f_{67}$	0.048930(50)	0.122(16)	4.62	$f_{15} - 4f_{51}$
$f_{68}$	4.926444(26)	0.1218(85)	8.90	side lobe	$f_{70}$	4.614637(27)	0.1203(85)	8.75	side lobe
$f_{71}$	0.015675(52)	0.120(17)	4.47	$f_{11} - f_{31}$	$f_{72}$	5.062966(27)	0.1193(85)	8.66	$f_{13} - 3f_{63}$
$f_{73}$	0.064300(52)	0.118(16)	4.51	$f_7 - f_{51}$	$f_{74}$	7.457145(21)	0.1179(66)	10.98	$f_{12} - f_{63}$
$f_{75}$	0.287801(48)	0.116(15)	4.86	side lobe	$f_{76}$	5.012063(28)	0.1161(85)	8.42	$f_3 + 9f_{26}$
$f_{77}$	0.455877(47)	0.114(14)	4.94	side lobe	$f_{78}$	1.543630(39)	0.112(11)	6.06	$f_6 - f_{63}$
$f_{79}$	7.820432(23)	0.1107(67)	10.28	$f_{13} + 8f_{16}$	$f_{80}$	5.913888(25)	0.1100(74)	9.25	$f_{12} - f_{31}$
$f_{81}$	16.311333(30)	0.1057(84)	7.80	side lobe	$f_{82}$	4.657617(30)	0.1054(85)	7.69	$f_1 - 102f_{\text{orb}}$
$f_{83}$	5.157936(31)	0.1053(85)	7.63	$f_{28} + 12f_{71}$	$f_{85}$	4.971226(31)	0.1037(85)	7.52	side lobe
$f_{86}$	3.184169(20)	0.1037(54)	11.83	side lobe	$f_{88}$	5.027535(32)	0.1015(85)	7.36	side lobe
$f_{89}$	7.431302(25)	0.0988(66)	9.20	$f_{36} + 65f_{\text{orb}}$	$f_{90}$	4.654931(32)	0.0985(85)	7.19	$f_{14} - f_{35}$
$f_{91}$	5.155692(33)	0.0980(85)	7.10	side lobe	$f_{92}$	1.513742(45)	0.098(12)	5.21	$f_{11} - f_{67}$
$f_{93}$	5.114072(33)	0.0972(85)	7.05	side lobe	$f_{94}$	5.111386(34)	0.0955(85)	6.92	$f_9 + f_{90}$
$f_{95}$	0.467336(57)	0.095(14)	4.12	$f_9 + 2f_{36}$	$f_{96}$	5.058205(34)	0.0936(85)	6.79	$f_{13} - 5f_{63}$
$f_{97}$	13.4290421(98)	0.0924(24)	23.92	$f_{16} + 28f_{95}$	$f_{98}$	2.979607(24)	0.0909(57)	9.84	$f_7 + 6f_{56}$
$f_{99}$	1.273069(56)	0.090(13)	4.20	$f_{12} - 4f_{31}$	$f_{100}$	4.569413(36)	0.0897(85)	6.55	side lobe
$f_{101}$	1.752612(46)	0.087(11)	5.07	$f_{12} - 3f_3$	$f_{102}$	5.068202(38)	0.0851(85)	6.18	$f_9 + f_{18}$
$f_{103}$	5.073507(39)	0.0829(85)	6.02	$f_7 + 6f_{65}$	$f_{104}$	4.924948(39)	0.0824(85)	6.02	side lobe
$f_{105}$	3.224768(25)	0.0820(54)	9.48	side lobe	$f_{106}$	16.310279(39)	0.0807(84)	5.95	side lobe
$f_{107}$	1.485247(55)	0.080(12)	4.23	$f_{15} + 7f_{\text{orb}}$	$f_{108}$	7.669935(33)	0.0776(67)	7.17	$f_{33} + 22f_{\text{orb}}$
$f_{109}$	5.157188(43)	0.0757(85)	5.49	side lobe	$f_{110}$	2.317604(50)	0.0751(99)	4.71	$f_{55} - 45f_{\text{orb}}$
$f_{111}$	8.096399(32)	0.0750(64)	7.27	$f_{60} + 43f_{\text{orb}}$	$f_{112}$	4.972688(43)	0.0745(85)	5.40	side lobe
$f_{113}$	4.958475(44)	0.0739(85)	5.36	$f_{16} + f_{27}$	$f_{114}$	2.125964(51)	0.0738(100)	4.58	$f_3 + f_7$
$f_{115}$	4.700767(44)	0.0728(85)	5.33	$f_{28} - 4f_{54}$	$f_{116}$	5.019000(44)	0.0724(85)	5.26	side lobe
$f_{117}$	3.268462(28)	0.0715(54)	8.26	$f_{114} + 10f_{\text{orb}}$	$f_{118}$	3.182367(29)	0.0714(54)	8.15	$f_{60} - f_{63}$
$f_{119}$	4.967995(46)	0.0702(85)	5.09	side lobe	$f_{120}$	7.818358(36)	0.0700(67)	6.50	$f_{13} + 6f_{35}$
$f_{121}$	14.765935(15)	0.0695(28)	15.26	$f_1 - f_6$	$f_{122}$	9.040388(24)	0.0695(44)	9.74	$f_5 + 5f_{61}$
$f_{123}$	2.979131(31)	0.0694(57)	7.51	side lobe	$f_{124}$	9.365388(22)	0.0688(40)	10.55	$f_6 + f_{79}$

**Table A1** continued on next page

**Table A1** (*continued*)

ID	Freq.(d <sup>-1</sup> )	Ampl.(mmag)	S/N	Remark	ID	Freq.(d <sup>-1</sup> )	Ampl.(mmag)	S/N	Remark
$f_{125}$	7.732704(37)	0.0683(67)	6.35	$f_5+4f_{38}$	$f_{126}$	5.012641(48)	0.0672(85)	4.88	side lobe
$f_{127}$	7.262682(38)	0.0670(68)	6.10	$f_{16}+31f_7$	$f_{128}$	4.356079(48)	0.0661(83)	4.90	$f_7+9f_{56}$
$f_{129}$	11.720940(16)	0.0646(27)	15.04	$f_3+44f_7$	$f_{130}$	2.738969(43)	0.0639(73)	5.43	$f_{124}-58f_{\text{orb}}$
$f_{131}$	5.0011556(51)	0.0635(85)	4.60	$f_{16}+f_{82}$	$f_{132}$	8.097521(38)	0.0633(64)	6.14	$f_{13}+2f_{92}$
$f_{133}$	7.480675(40)	0.0632(67)	5.83	$f_{12}+4f_{36}$	$f_{134}$	5.014375(52)	0.0625(85)	4.53	side lobe
$f_{135}$	5.105979(52)	0.0622(85)	4.51	$f_{14}-3f_{63}$	$f_{136}$	4.615623(52)	0.0617(85)	4.49	$f_{113}-3f_{\text{orb}}$
$f_{137}$	17.855813(14)	0.0594(23)	16.29	$f_1+f_6$	$f_{138}$	3.184747(35)	0.0582(54)	6.64	$f_{32}+15f_{51}$
$f_{139}$	3.225652(35)	0.0572(54)	6.61	side lobe	$f_{140}$	6.928637(45)	0.0569(67)	5.23	$f_3+f_{87}$
$f_{141}$	5.062082(57)	0.0566(85)	4.11	side lobe	$f_{142}$	4.862552(56)	0.0565(84)	4.16	$f_7+3f_{31}$
$f_{143}$	4.882886(57)	0.0560(84)	4.13	$f_{94}-2f_{\text{orb}}$	$f_{144}$	5.113392(58)	0.0559(85)	4.05	side lobe
$f_{145}$	9.394903(27)	0.0558(40)	8.59	$f_5+f_{125}$	$f_{146}$	6.635804(43)	0.0554(63)	5.41	$f_{11}+f_{103}$
$f_{147}$	4.854698(57)	0.0552(84)	4.06	$f_{28}-f_{\text{orb}}$	$f_{148}$	4.241761(57)	0.0546(83)	4.07	$f_{128}-f_{\text{orb}}$
$f_{149}$	7.850966(46)	0.0543(66)	5.06	$f_{14}+6f_9$	$f_{150}$	3.681427(43)	0.0541(62)	5.43	$f_9+f_{58}$
$f_{151}$	11.500193(19)	0.0531(27)	12.09	$f_{11}+2f_{28}$	$f_{152}$	7.457621(48)	0.0524(66)	4.88	side lobe
$f_{153}$	2.980049(41)	0.0523(57)	5.66	side lobe	$f_{154}$	2.738459(53)	0.0514(73)	4.37	side lobe
$f_{155}$	7.482953(50)	0.0512(67)	4.72	$f_{12}+10f_{63}$	$f_{156}$	7.428582(50)	0.0502(66)	4.68	$f_{12}-2f_{71}$
$f_{157}$	3.268972(40)	0.0501(54)	5.79	side lobe	$f_{158}$	6.946965(51)	0.0495(67)	4.55	$f_{12}-8f_{73}$
$f_{159}$	9.063374(34)	0.0495(44)	6.97	$f_{151}-4f_{37}$	$f_{160}$	9.288984(31)	0.0495(41)	7.45	$f_{12}+3f_{37}$
$f_{161}$	3.820601(49)	0.0492(63)	4.79	$f_{28}-4f_{43}$	$f_{162}$	3.821349(49)	0.0490(63)	4.77	side lobe
$f_{163}$	7.819820(52)	0.0481(67)	4.47	side lobe	$f_{164}$	6.305364(45)	0.0473(56)	5.19	$f_4-12f_{65}$
$f_{165}$	14.403056(21)	0.0471(26)	11.27	$f_{14}+f_{160}$	$f_{166}$	9.396093(32)	0.0469(40)	7.22	$f_6+f_{149}$
$f_{167}$	7.319943(56)	0.0453(67)	4.16	$f_{12}-9f_{71}$	$f_{168}$	3.183013(46)	0.0444(54)	5.07	side lobe
$f_{169}$	6.926223(58)	0.0439(67)	4.04	$f_{12}-8f_{54}$	$f_{170}$	3.793637(54)	0.0438(63)	4.29	$f_{15}+9f_{26}$
$f_{171}$	7.340991(58)	0.0437(67)	4.04	$f_{16}+44f_{51}$	$f_{172}$	3.640488(50)	0.0436(58)	4.63	$f_9+f_{60}$
$f_{173}$	9.397589(35)	0.0435(40)	6.69	$f_{15}+2f_{128}$	$f_{174}$	3.620868(51)	0.0427(58)	4.57	$f_{135}-13f_{\text{orb}}$
$f_{175}$	8.091639(57)	0.0419(64)	4.06	$f_5+14f_{56}$	$f_{176}$	3.639944(53)	0.0418(58)	4.44	side lobe
$f_{177}$	3.822063(58)	0.0414(63)	4.04	$f_{14}-15f_{44}$	$f_{178}$	6.328588(53)	0.0403(57)	4.41	$f_{23}+11f_{\text{orb}}$
$f_{179}$	3.183557(51)	0.0399(54)	4.56	side lobe	$f_{180}$	6.331410(54)	0.0398(57)	4.36	$f_{14}+2f_{37}$
$f_{181}$	6.307914(54)	0.0395(56)	4.32	$f_1-2f_{131}$	$f_{182}$	3.224258(52)	0.0388(54)	4.48	side lobe
$f_{183}$	18.213762(20)	0.0377(20)	11.58	$f_1+f_3$	$f_{184}$	9.006555(45)	0.0374(44)	5.21	$f_{12}+f_{31}$
$f_{185}$	8.492431(56)	0.0372(55)	4.18	$f_{37}+69f_{\text{orb}}$	$f_{186}$	3.267986(56)	0.0363(54)	4.20	side lobe
$f_{187}$	11.723354(28)	0.0362(27)	8.43	$f_7+f_{151}$	$f_{188}$	3.226706(56)	0.0362(54)	4.18	$f_{166}-54f_{\text{orb}}$
$f_{189}$	18.257354(21)	0.0360(20)	11.12	$f_{11}+11f_{38}$	$f_{190}$	8.530583(58)	0.0349(54)	4.01	$f_5+15f_{35}$
$f_{191}$	3.447827(58)	0.0345(53)	4.02	$f_3+f_6$	$f_{192}$	9.367870(45)	0.0339(40)	5.20	$f_9+6f_{107}$
$f_{193}$	11.497779(31)	0.0334(27)	7.60	$f_1-14f_{16}$	$f_{194}$	9.289630(47)	0.0329(41)	4.96	side lobe
$f_{195}$	8.805122(58)	0.0320(49)	4.05	$f_{167}+13f_{\text{orb}}$	$f_{196}$	8.926036(55)	0.0311(45)	4.24	$f_{122}-f_{\text{orb}}$
$f_{197}$	9.366340(49)	0.0310(40)	4.75	side lobe	$f_{198}$	9.393202(51)	0.0299(40)	4.60	$f_{32}+25f_{16}$
$f_{199}$	9.3633416(51)	0.0296(40)	4.53	$f_1-f_{158}$	$f_{200}$	14.643762(34)	0.0295(27)	6.81	$f_{28}+3f_{58}$
$f_{201}$	9.028079(58)	0.0289(44)	4.04	$f_{156}+14f_{\text{orb}}$	$f_{202}$	11.721552(36)	0.0277(27)	6.44	side lobe
$f_{203}$	11.720090(36)	0.0277(27)	6.44	side lobe	$f_{204}$	9.417073(55)	0.0276(40)	4.27	$f_5+17f_9$
$f_{205}$	9.394325(55)	0.0274(40)	4.21	side lobe	$f_{206}$	11.106405(40)	0.0269(28)	5.87	$f_{181}+42f_{\text{orb}}$
$f_{207}$	17.972987(31)	0.0260(21)	7.48	$f_{72}+113f_{\text{orb}}$	$f_{208}$	9.727995(54)	0.0255(36)	4.35	$f_{13}+f_{82}$
$f_{209}$	14.620130(43)	0.0232(27)	5.39	$f_{13}+3f_{60}$					

NOTE—<sup>a</sup> The  $\simeq$  in the Remark column of  $f_{18}$  is because the difference is about 0.005, which is greater than  $1.5/T_{\text{span}}$ .